mathematics

MDPI

Article

The Effect of Preloaded Compressive Stress and Curvature of Defect on Blast-Induced Fracture Behavior by Caustic and Numerical Models

Chen Huang [1,2], Zong-Xian Zhang [2], Adeyemi Aladejare [2], Xianbo Guan [2], Bingbing Yu [1] and Liyun Yang [1,*]

[1] School of Mechanics and Civil Engineering, China University of Mining and Technology-Beijing, Beijing 100083, China; huangchen4510@sina.com (C.H.); bqt2200604037@student.cumtb.edu.cn (B.Y.)
[2] Oulu Mining School, University of Oulu, 90570 Oulu, Finland; zongxian.zhang@oulu.fi (Z.-X.Z.); adeyemi.aladejare@oulu.fi (A.A.); xianbo.guan@student.oulu.fi (X.G.)
* Correspondence: yangly@cumtb.edu.cn

Abstract: In this study, the effects of preloaded uniaxial compressive stress and defect (prefabricated by laser cutting) curvature on blast-induced cracks and stress wave propagation were investigated in polymethyl methacrylate (PMMA) specimens using caustics theory. Based on the mathematical relationship between stress and optics, the fracture behavior (the propagation path, dynamic stress intensity factors (DSIFs), propagation velocity, initiation angle of the main crack, and damage degree between the defect and the blasthole) was calculated and analyzed quantitatively. The results show that the preloaded stress could mainly restrain the main crack propagation in the horizontal direction and reduce the initiation angle and damage degree at the defects. Meanwhile, the crack initiation position of the positive curvature defect was not at the end of the defect. In addition, the curvature of the defect significantly affected the blast-induced fracture compared to preloaded stresses. Comparing the main crack with other curvature defects, the DSIFs, velocity, crack arrest time, crack length, and horizontal offset distance of the main crack with negative curvature defect were the largest. The variation in the full stress field in the specimen under blasting and preloaded stress was simulated by a numerical model. The results show that the curvature of the defect has a significant effect on tensile waves at the end of defects, and the tensile stress from high to low was C_{-25}, C_0, and C_{25}, in that order.

Keywords: blast; preloaded compressive stress; defect; crack propagation; stress intensity factors

MSC: 74R10

Citation: Huang, C.; Zhang, Z.-X.; Aladejare, A.; Guan, X.; Yu, B.; Yang, L. The Effect of Preloaded Compressive Stress and Curvature of Defect on Blast-Induced Fracture Behavior by Caustic and Numerical Models. *Mathematics* **2023**, *11*, 4532. https://doi.org/10.3390/math11214532

Academic Editor: Andrey Jivkov

Received: 18 October 2023
Revised: 27 October 2023
Accepted: 30 October 2023
Published: 3 November 2023
Corrected: 8 May 2024

1. Introduction

Blasting is a traditional and effective construction method, which is widely used in tunnelling, mining, and other types of hard rock engineering [1,2]. Since rock or rock-like materials contain inherent defects (such as holes, joints, and cracks), such defects affect stress wave propagation, and thereby influence fracture mode and crack propagation in the materials [3–5]. The shape of the defect, including its length, curvatures, and radius, is an important factor that directly affects the dynamic fracture [6,7]. Also, as underground engineering goes deeper, the in situ stresses, often compressive, significantly affect blast-induced fracture and blasting results. Hence, there is need to study the fracture behavior of a blast-induced crack under preloaded stress [8–11]. In addition, it is necessary to investigate how a preloaded static stress and the defect curvature affect blast-induced fracture of the medium.

Numerous studies of blast-induced fracture in media with defects have been widely carried out, mainly on the geometric shape and size [12,13], quantity [14], inclination [15], and characteristics of defects [16]. For example, Li et al. [12] performed the blasting experiment in a polymethyl methacrylate (PMMA) specimen with double vertical defects.

The results show that the initiation angle, final propagation length, and initiation time of the end crack increase with the increase in defect length. Additionally, Zhu et al. [13] investigated the influence of joint filling material, width, and location on the blast-induced failure. Atmane et al. [17–21] explored the behavior of stress wave propagation in media with holes based on a variety of theories. Furthermore, some scholars have carried out research on arc defects. For example, Ding et al. [22] explored the interaction process between directional cracks in slotted blasting and three types of open joints (straight, ellipses and circles), indicating that open joints block the propagation of directional cracks. Li et al. [23] investigated the influence of the radius of defect curvature on the blast-induced crack in retained medium. However, the study did not analyze how curvature affected the end of the defect or how the medium was damaged on the blasting side.

For blasting under preloaded static stress field, many scholars explained that the preloaded stress affects blast-induced fracture and stress waves [7–9,24,25]. The preloaded stress could change the stress state around the blasthole, and thereby affect the damage and crack distribution around the blasthole. In addition, the preloaded stress had a guiding effect on blast-induced cracks, and the main crack propagated along the direction of the maximum principal stress [26]. Some studies found that preloaded stress can promote the propagation of blast-induced cracks parallel to the principal stress and inhibit the propagation of cracks perpendicular to the principal stress [27]. For the study of media with defects under preloaded stress, Zhou et al. [28] calculated the tip dynamic coefficient of a parallel crack under combined preloaded and dynamic stresses, and analyzed the influence of preloaded stress and crack geometric parameters on the dynamic response theoretically. Yang et al. [29,30] carried out blasting experiments on PMMA specimens, and the influence of preloaded stress on the blast-induced crack of the medium with straight defects was studied. The results show that the preloaded stress affects the crack initiation and increases the shear failure at the end of the defect.

Numerical analysis is also an effective method to explore the blast-induced fracture of a medium with defects under preloaded stress and stress waves [31–33]. For example, Wei [26] carried out a numerical simulation of double-hole blasting in media with defects under preloaded stress and studied the penetration of blast-induced cracks under different preloaded stress and defect angles. The results show that the compressive stress prevents the occurrence of blast-induced cracks, but the defect guides the crack propagation along the defect. Wang et al. [32] explored the effect of in situ stress and freedom on the fracture process of medium by the coupling method of LS-DYNA and UDEC. Li et al. [33] performed a numerical simulation of blasting in a medium with defects and a weak face by LS-DYNA. It was found that the tensile stress between the blasthole and the defect is maximum when the lateral pressure coefficient is 1.33. Experimental research on the influence of preloaded stress and defects on blast-induced fracture is rarely reported in the literature.

As a result of the literature review above, it is noted that most of the blasting studies under the coupling action of defects and preloaded stress is mostly based on numerical simulation methods, with no reported study on experimental methods. In addition, most of the blasting studies focused on linear defects, but there were few studies on bending defects. In addition, the effects of defects on stress wave and dynamic fracture were rarely studied from the perspective of preloaded stress and curvature. In this study, the blast-induced fracture behavior in specimens with arc defects under preloaded compressive stress was studied by caustics system. The effects of preloaded stress and defect curvature on propagation of cracks were explored, and the blast-induced damage in each specimen were analyzed. In addition, the mechanism of a defect crack under different curvatures was explained. Finally, the stress wave propagation with different curvature defects was analyzed by LS-DYNA (R 18.0) software.

2. Experimental System

2.1. Specimen

The caustic method was used and the PMMA was employed in experiments because of its good mechanical properties and transparency. Therefore, most caustic blasting tests were conducted on PMMA samples, and cracks can be easily seen in these samples [9,10,14]. Table 1 displays the PMMA parameters.

Table 1. The parameters of PMMA [26,34].

Elastic Modulus/E_d	Poisson's Ratio/v	Optical Constant/c	Velocity of Transverse Wave/v_s	Velocity of Longitudinal Wave/v_p	Density/ ρ
3.595 GPa	0.32	1.08 GPa^{-1}	1090 m/s	2125 m/s	1.17 g/cm^3

In Figure 1, the specimen is 315 mm × 285 mm × 6 mm in size, with a central round hole and a line defect. The defect and a round hole were prefabricated by laser cutting. The radius of the central round hole is 2 mm and is used as a blasthole. The length of the prefabricated defect is 50 mm. The primary goal of this research is to explore the crack propagation behavior of the defect tip, so the distance between the defect tip and the blasthole is the same, which is 40 mm. Three groups of specimens (group A, group B, and group C) were designed with defect curvature as variables. The defect curvatures in the three groups of specimens are $-25\ m^{-1}$, $0\ m^{-1}$, and $25\ m^{-1}$, and were named C_{-25}, C_0, and C_{25}, respectively. Preloaded compressive stress (p_1 = 0 Mpa or 3 Mpa) was applied on the lower and upper sides of the specimen. The experimental scheme is shown in Table 2.

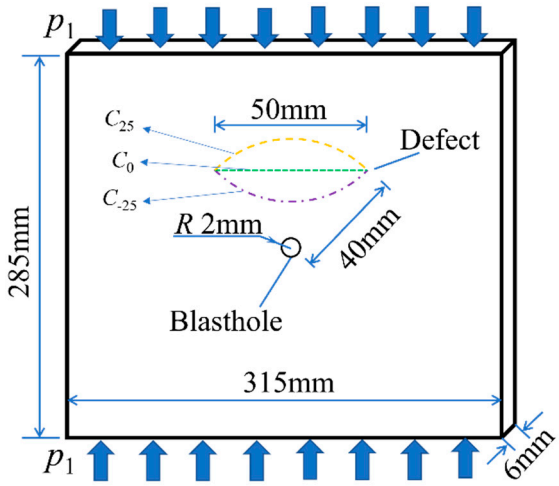

Figure 1. Specimen model showing the defects with different curvatures (C_{-25}, C_0, and C_{25}) in the specimen.

Table 2. Experimental scheme design.

Specimens No.	Compressive (MPa)	Curvature (m^{-1})	Specimens No.	Compressive (MPa)	Curvature (m^{-1})
A1	0	−25	A2	3	−25
B1	0	0	B2	3	0
C1	0	25	C2	3	25

2.2. Caustic System

The caustic method is an optical mechanics experimental approach that is commonly utilized in dynamic fracturing produced by blasting and impact [6,7]. The schematic diagram of the optical measuring equipment in this experiment is shown in Figure 2a [3]. A

laser with a wavelength of 532 nm was used as a point light source; a beam expander and a convex lens were used to produce collimated light; the collimated light passed through the specimen and field lens 2 and finally converged at the camera. The specimen should be perpendicular to the collimated light. The focused surface of a camera is defined as a reference plane. The distance Z0 between the specimen's surface and the reference plane is 1200 mm, which is of critical importance for the measurement of caustics.

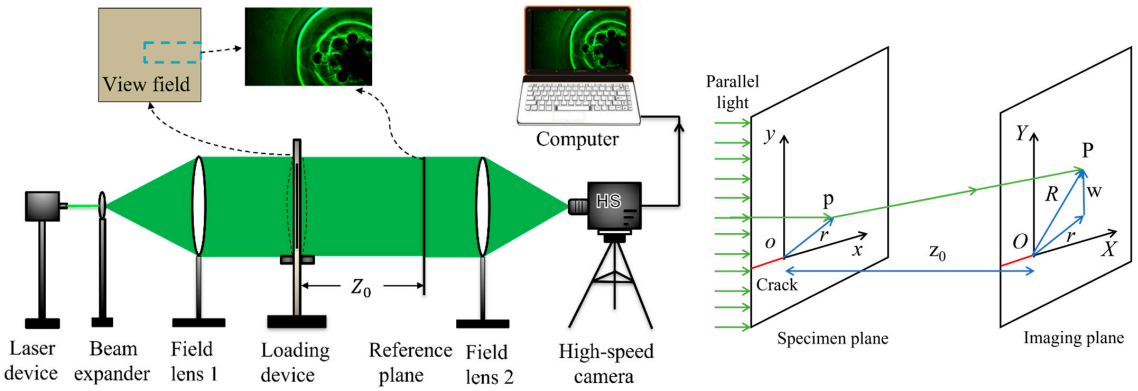

(**a**) (**b**)

Figure 2. The caustic method. (**a**) A caustic experimental system. (**b**) Mathematical derivation diagram [35].

A camera (FASTCAM SA5, Photron, Japan) was used to capture caustic images. This camera is characterized by a higher shooting rate corresponding to a smaller field of view. Here, the camera used a post-trigger mode with a frame rate of 140,000 and an exposure time of 1,000,000.

2.3. Calculation Method of Dynamic Stress Intensity Factors (DSIF) and Crack Velocity

The caustic method is an experimental method that uses geometric optics to convert image information into clear shadow optical patterns [34]. When an external load is applied, the sample thickness and the refractive index of the material change near the force deformation zone, and these changes will change the light propagation direction. When a bundle of parallel light deviates from the parallel state due to stress changes, a three-dimensional envelope surface forms in the space, and this envelope surface acts as a caustic surface. If a reference plane parallel to the plane of the component is placed at a certain distance from the model, the cross section of the caustic surface can be directly observed. Within the cross-sectional image, a dark area without light is enclosed. The bright line is the area of the caustics, and the dark area is the shadow spot. The following references are from P. Qiu [35], P.S. Theocaris [36], A.J. Rosakis [37] and G.A. Papadopoulos [38].

According to Econal theory, the deflection vector produced by parallel light passing through the crack tip region can be expressed as Equation (2) [38].

$$\mathrm{w} = -z_0 \mathrm{grad} s(x, y) \tag{1}$$

where z_0 is the distance between the reference plane and the specimen; $s(x, y)$ represents a light surface.

When the light passes through the specimen vertically, Equation (1) can be simplified to Equation (2).

$$\mathrm{w} = -z_0 \mathrm{grad} \Delta s(x, y) \tag{2}$$

where $\Delta s(x, y)$ is the optical path difference caused by light passing through the crack tip region.

According to the Maxwell–Neumann principle, the optical path difference can be associated with the stress state of the crack tip [35,37].

$$\Delta s(x,y) = cd[(\sigma_1 + \sigma_2) + \xi(\sigma_1 - \sigma_2)] \tag{3}$$

where c is the optical constant; σ_1 and σ_2 are the principal stresses. ξ represents the stress coefficient of anisotropic materials. The PMMA specimen belongs to isotropic material, so ξ is 0 for PMMA specimen.

According to the Mohr stress circle, $\sigma_1 + \sigma_2 = \sigma_{xx} + \sigma_{yy}$.

$$\Delta s(x,y) = cd(\sigma_{xx} + \sigma_{yy}) \tag{4}$$

Considering the crack velocity, the dynamic stress field at the crack tip can be expressed as Equations (5)–(7) [35].

$$\sigma_{xx} = \frac{K_1^d(t)}{\sqrt{2\pi}} \times B_l(v)\left[\left(1 + 2\alpha_l^2 - \alpha_s^2\right)\frac{\cos(\theta_l/2)}{r_l^{1/2}} - \frac{4\alpha_l\alpha_s}{(1+\alpha_s^2)}\frac{\cos(\theta_s/2)}{r_s^{1/2}}\right] \tag{5}$$

$$\sigma_{yy} = \frac{K_1^d(t)}{\sqrt{2\pi}} \times B_l(v)\left[-\left(1 + \alpha_s^2\right)\frac{\cos(\theta_l/2)}{r_l^{1/2}} + \frac{4\alpha_l\alpha_s}{(1+\alpha_s^2)}\frac{\cos(\theta_s/2)}{r_s^{1/2}}\right] \tag{6}$$

$$\tau_{xy} = \frac{K_1^d(t)}{\sqrt{2\pi}} \times 2B_l(v)\alpha_l\left[\frac{\sin(\theta_l/2)}{r_l^{1/2}} - \frac{\sin(\theta_s/2)}{r_s^{1/2}}\right] \tag{7}$$

$$r_l e^{l\theta_l} = x_l + iy_l = x + i\alpha y \tag{8}$$

$$\alpha_l = \left(1 - v^2/v_\rho^2\right)^{1/2}, \alpha_s = \left(1 - v^2/v_s^2\right)^{1/2} \tag{9}$$

where v_p and v_s are shown in Table 1.

$$B_l(v) = \frac{\left(1 + \alpha_s^2\right)}{4\alpha_l\alpha_s - \left(1 + \alpha_s^2\right)^2} \tag{10}$$

According to the above equation, the sum of the principal stress can be obtained.

$$\begin{aligned}\sigma_{xx} + \sigma_{yy} &= \frac{K_1^d(t)B_l(v)}{\sqrt{2\pi}}\left(2\alpha_l^2 - 2\alpha_s^2\right)\frac{\cos(\theta_l/2)}{r_l^{1/2}} \\ &= K_1^d(t)\frac{\left(1+\alpha_s^2\right)\left(\alpha_l^2-\alpha_s^2\right)}{4\alpha_l\alpha_s-\left(1+\alpha_s^2\right)^2}\sqrt{\frac{2}{\pi r_l}}\cos(\theta_l/2)\end{aligned} \tag{11}$$

The corresponding relationship between the position of light deflection P (X, Y) and $p(x_l, y_l)$ on the plane of the specimen can be established.

$$\begin{aligned}X &= r_l\cos\theta_l + Cr_l^{-3/2}\cos\tfrac{3\theta_l}{2} \\ Y &= \tfrac{r_l\sin\theta_l}{\alpha_l} + \alpha_l Cr_l^{-3/2}\sin\tfrac{3\theta_l}{2}\end{aligned} \tag{12}$$

$$C = \frac{z_0 cdK_l^d}{F(v)\sqrt{2\pi}} \tag{13}$$

$F(v)$ is the speed adjustment factor, which can be calculated as Equation (14).

$$F(v) = \frac{4\alpha_l\alpha_s - \left(1 + \alpha_s^2\right)^2}{(1 + \alpha_s^2)(\alpha_l{}^2 - \alpha_s^2)} \tag{14}$$

Here, we can find that the initial curve of the caustic is

$$r_0 = \left(\frac{3}{2}CR\right)^{2/5} \tag{15}$$

$$R = \frac{1}{2}\left(1-\alpha_l^2\right)\cos\frac{5\theta_l}{2} + \frac{1}{2}\left[\left(1-\alpha_l^2\right)\cos\frac{5\theta_l}{2} + 4\alpha_l^2\right]^{1/2} \tag{16}$$

By substituting Equation (15) into Equation (12), the caustic curve of the theory can be obtained.

$$\begin{aligned} X &= \left(\tfrac{3}{2}CR\right)^{2/5}\left[R^{2/5}\cos\theta_l + \tfrac{2}{3}R^{-3/5}\cos\tfrac{3\theta_l}{2}\right] \\ Y &= \left(\tfrac{3}{2}CR\right)^{2/5}\left[\tfrac{R^{2/5}}{\alpha_l}\sin\theta_l + \tfrac{2}{3}\alpha_l R^{-3/5}\sin\tfrac{3\theta_l}{2}\right] \end{aligned} \tag{17}$$

The caustic spot of type I is symmetrical along the crack propagation direction, and the $D_{\max}$ can only be obtained by deriving the θ_l from Equation (17). Therefore, the DSIF can be calculated according to the caustics size, and the calculation method is shown in Equation (18) [18,22,25,29].

$$K_{\mathrm{I}} = \frac{2\sqrt{2\pi}F(v)}{3g^{5/2}z_0 c d_{\mathrm{eff}}} D_{\max}^{5/2} \tag{18}$$

where K_{I} is DSIF; g is the DSIF coefficient, which is 3.17; $D_{\max}$ is the maximum diameter of the caustics; d_{eff} is the specimen's thickness.

The position of the spot at any time can be obtained from the caustics picture, and the center of the spot is roughly the position of the crack tip. Therefore, the crack velocity calculated by the adjacent images is taken as the instantaneous velocity. The crack instantaneous velocity is calculated as:

$$v_x \approx \frac{\Delta l_x}{\Delta t},\ v_y \approx \frac{\Delta l_y}{\Delta t}, v = \sqrt{\left(v_x^2 + v_y^2\right)} \tag{19}$$

where Δl_{x} and Δl_{y} are the horizontal and vertical displacement differences; v_{x} and v_{y} are the horizontal and vertical velocities. Δt is the time between the two consecutive caustic photos, which is 7.14 μs in this study. v is crack velocity.

2.4. Loading System

As shown in Figure 3, preloaded compressive stress and dynamic load are applied by the loading system [34]. The jack was placed between the moving support and the reaction force frame. The compressive stress was imparted to the specimen by pushing down the moving support. A stress sensor with an accuracy of 0.1 kg and a range of 5 *t* was placed between the jack and the reaction shelf to measure the preloaded stress applied to the specimen, considering the self-weight of the jack and the moving bearing. The specimen was put into a card slot to prevent out-of-plane deformation. At the same time, lubricating oil was used around the specimen to reduce friction, making it easy for the specimen to move up and down. Coupling charge is used in the study. The self-designed drug pack (lead azide) was put into the blasthole fixed by the fixture to realize dynamic loading.

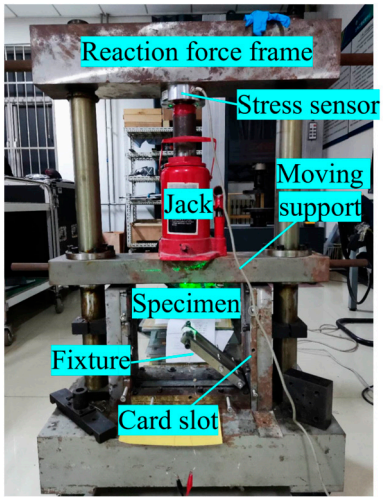

Figure 3. The loading system. The system includes a reaction force frame, a stress sensor, a jack, a moving support, a card slot, and a fixture.

3. Experimental Results

3.1. The Crack at the End of Defects

Figure 4 shows the distribution of blast-induced cracks in specimens with different curvature defects under different compressive stresses. Except for group C, there was a long blast-induced crack at the end of the defect in group A and group B. There was no crack at the end of the defect in specimen C1, but blast-induced cracks occurred in the non-end position in specimen C2. In this experiment, the crack at the end of the defect was defined as the main crack, and one main crack in each group of specimens was selected as the research object. Furthermore, the Cartesian coordinate system was built, taking the manufactured defect's end as the origin, as shown in Figure 4. The lengths of the crack tips in the x and y directions were measured, and the maximum offset distance of the main crack and crack initiation position in the x direction were also recorded, as shown in Table 3.

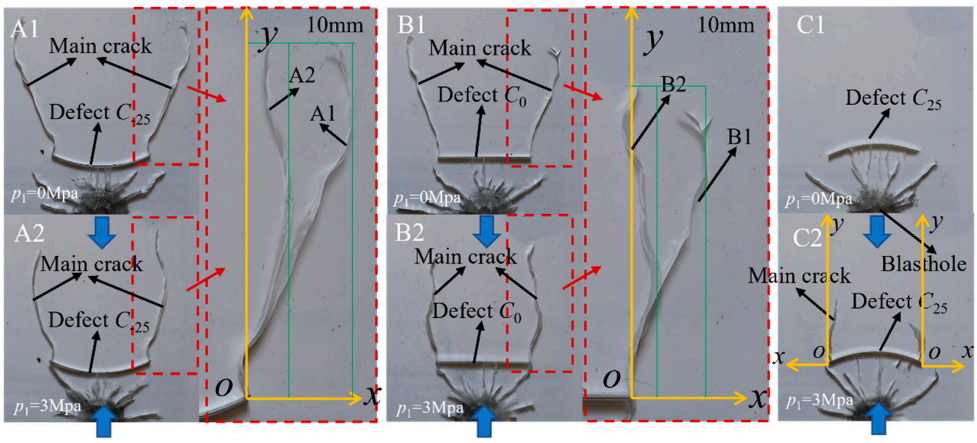

Figure 4. Specimens after blasting. *O* is the end position of the defect. The green line represents the maximum offset distance of the crack. The specimens (A1, B1, C1) were not subjected to static stress. The specimens (A2, B2, C2) were subjected to 3 Mpa stress (Blue arrow).

Table 3. Crack propagation length and initiation position.

Specimens No.	Length-*x* /mm	Length-*y* /mm	Maximum Offset-*x*/mm	Crack Initiation Position-*x*/mm
A1	16.7	68.0	19.9	0
A2	4.3	66.9	8.6	0
B1	10.3	58.8	15.3	0
B2	1.3	62.7	5.4	0
C1	0	0	0	0
C2-1	2.5	32.6	2.5	1.8
C2-2	3.9	19.9	3.9	1.8

In group A, the maximum offset distance of the main crack in specimen A2 (8.6 mm) is less than that in specimen A1 (19.9 mm), and the offset distance of the crack tip in specimen A2 (4.3 mm) is less than that in specimen A1 (16.7 mm). The crack path in group B is similar to that in group A. The maximum offset distances of the main cracks in specimens B1 and B2 were 15.3 mm and 5.4 mm, respectively. The offset distances of the crack tip in specimens A1 and A2 were 10.3 mm and 1.3 mm, respectively. There was no main crack in specimen C1, so the main cracks in specimens C1 and C2 were no longer compared. The results show that the compressive stress can significantly restrain the propagation of the main crack in the horizontal direction. At the same time, it is found that for the specimens with the same curvature, the coincidence degree of the explosive crack propagation path is higher in the first half. The horizontal distance between the two cracks increases with the increase in the propagation length, showing that the preloaded stress has little effect on blast-induced crack propagation in the early stage, but the influence of preloaded stress on crack propagation increases gradually with the dissipation of energy.

Comparing the y direction length in the same group of specimens, the y direction length in specimen B1 is slightly larger than that in specimen B2. However, for the two specimens in group A, the crack lengths in the y direction are close to each other, being 68 mm and 66.9 mm, respectively. The findings demonstrate that the preloaded stress has little influence on the crack in the y direction. By observing the morphology of the main cracks in specimens A2 and B2, it is found that the crack path is not straight (bending path) under the boundary-reflected wave. Previous studies show that the influence of preloaded stress on crack propagation depends on its propagation direction [27]. Therefore, the preloaded compressive stress affects the final crack length by its propagation path.

To explore the effect of curvature on the main crack propagation under preloaded stress, specimens A2, B2, and C2 were selected for comparison. The maximum offset distances in the three groups of specimens were 8.6 mm, 5.4 mm, and 2.5 mm (3.9mm), respectively. Moreover, the crack lengths in the y direction were 66.9 mm, 62.7 mm, and 32.6 mm (19.9 mm), respectively. The results indicate that curvature of the defect significantly affects the crack propagation in the horizontal and vertical direction, that is, specimen A2 (C_{-25}) > specimen B2 (C_0) > specimen C2 (C_{25}). The crack initiation position in group A and group B was at the end of the defect, but the initiation position in specimen C2 is on the arc defect, which is 1.8 mm away from the end. This indicates that the curvature of defects affects the initiation position of the main crack, and the end of the defect is no longer easy to crack when the curvature of the defect is positive (C_{25}). The phenomenon will be further explored in Section 4.

3.1.1. Caustics Picture

Figure 5 shows the dynamic caustic process in specimens with different curvature defects under preloaded stress, and the blast-induced fracture behavior is visualized. The propagation of the stress wave can be viewed by changing the light and dark stripes in the caustics. To explore the influence of preloaded compressive stress on crack propagation at the end of defects, this study only takes group B specimens (B1 and B2) as examples. Meanwhile, the effects of different curvatures on crack propagation under preloaded stress

are compared and analyzed by taking specimens A2, B2, and C2 as examples. Therefore, only caustics images of specimens A2, B1, B2, and C2 were exhibited in this study. From the caustics picture at t = 0 μs, the other three specimens produce compressed caustic spots at the end of the defect, except specimen B1. When stress waves met defects, the propagation direction of the stress wave changed and diffraction occurred along the end of the defect, and the blast-induced crack occurred and propagated rapidly. The caustic spots also represent the energy of the crack tip. The caustic spots in each group of specimens are mainly mode I, indicating that the fracture is mainly controlled by tensile stress. Meanwhile, at about 100 μs and 128 μs, the crack tip met the reflected wave, which would change the spot shape, size, and crack path. In the later stage of blasting, the caustic spots became smaller gradually, and finally, the crack stopped.

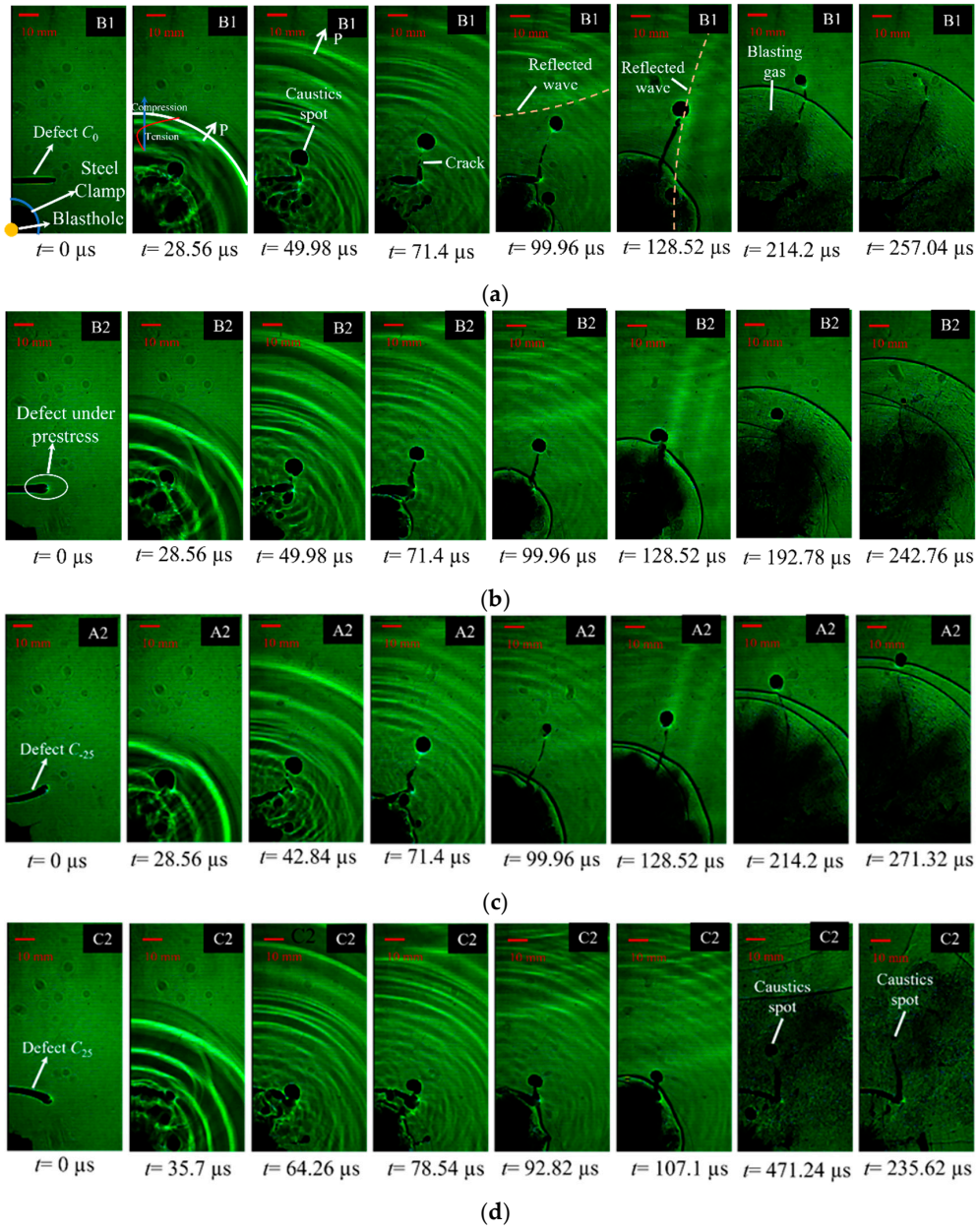

Figure 5. Caustics picture in blasting. (**a**) Specimen B1 (C_0, p_1 = 0 Mpa); (**b**) specimen B2 (C_0, p_1 = 3 Mpa); (**c**) specimen A2 (C_{-25}, p_1 = 3 Mpa); (**d**) specimen C2 (C_{25}, p_1 = 3 Mpa).

3.1.2. The DSIFs at Crack Tip

As shown in Figure 6, the curve of the DSIF in group B with time was drawn. The DSIFs of the two specimens decreased at first and then increased at the crack initiation stage. Then, the DSIFs decreased continuously with the continuous propagation of the crack. Between 100 μs and 128 μs, the crack met the first reflected stress wave, so the DSIFs increased sharply and then decreased. The two curves are relatively close, indicating that the preloaded stress has little influence on the DSIFs. The comparison of the curves in specimens B1 and B2 shows that the DSIFs in specimen B1 are larger than those in specimen B2 before the reflected waves (including the initiation stage). However, the DSIFs in specimen B2 are larger than those in specimen B1 in the later stage. The results suggest that the preloaded compressive stress can reduce the DSIFs in the early stage and promote the DSIFs with blast-induced stress wave attenuation. The propagation of the crack is towards the compressive stress direction. This phenomenon explains why the crack propagation is longer or shorter under preloaded stress. The influence of preloaded stress on the crack propagation depends on the crack direction. The angle between preloaded stress and crack propagation determines the ratio of inhibition or promotion, and affects the final crack length. Although the preloaded stress is parallel to the crack propagation direction, the DSIFs in specimen B2 are less than those in specimen B1 in the early stage (50–100 μs). From this phenomenon, it can be inferred that the DSIFs at crack initiation has a significant impact on the DSIFs in propagation due to the inertia effect, and the preloaded stress also has a lag effect on the blast-induced fracture.

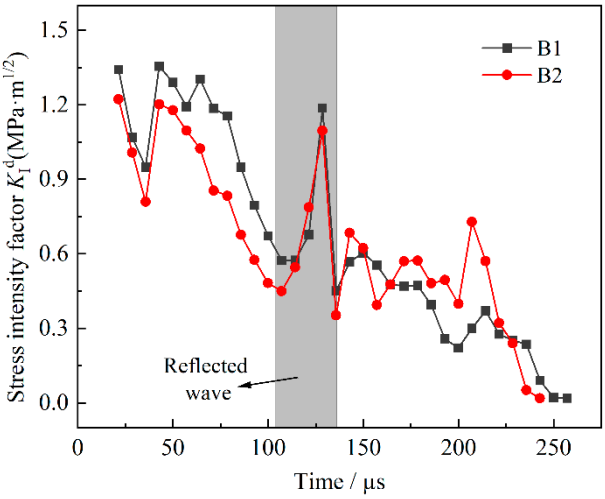

Figure 6. The DSIFs in group B with time. The grey part is the stage when the reflected wave meets the crack.

To study the effect of curvature on the DSIFs under preloaded stress, the curve of the DSIFs in specimens A2, B2, and C2 with time was drawn, as shown in Figure 7. The figure shows that the changing trend of DSIFs at the crack tip in each specimen is similar to that in group B. Except during the action of reflected waves, the DSIFs in each specimen from large to small are specimen A2, specimen B2, and specimen C2, indicating that the curvature of the defect significantly affects the DSIFs of the crack tip. According to the experimental results, it can be inferred that the DSIFs in the specimen with a negative curvature defect are larger than those in the specimen with a positive curvature defect. Because the main crack propagation length is different when it encounters the reflected wave in the specimen with different curvature defect, the DSIFs is also different. The slope of the DSIFs curve is defined as the crack tip loading rate [39]. In the attenuation stage, after crack initiation, the crack tip loading rates in specimens A2, B2, and C2 are -2.0×10^4 MPa·m$^{1/2}$·s^{-1}, -1.3×10^4 MPa·m$^{1/2}$·s^{-1}, and -1.1×10^4 MPa·m$^{1/2}$·s^{-1}, respectively. The findings indicate that the curvature of the defect affects the attenuation rate

of the DSIFs. The attenuation rates from large to small are specimen A2 (C_{-25}), specimen B2 (C_0), and specimen C2 (C_{25}).

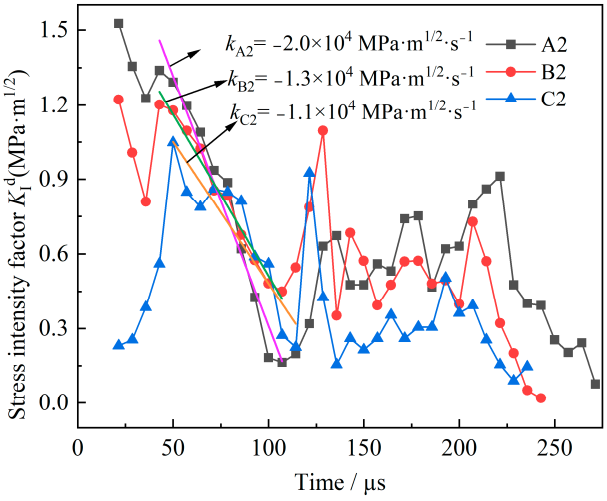

Figure 7. The DSIFs in specimens with different curvature vs. time.

3.1.3. Crack Propagation Velocity

Figure 8 shows that the horizontal velocity v_x and vertical velocity v_y change with time in group B. The horizontal velocity v_x affects the crack offset. In the two specimens, the horizontal velocity v_x oscillates up and down along the zero axis. The curves of the two specimens are similar in the early stage, but different in the later stage. This is because the crack propagation direction is mainly controlled by stress waves, but the preloaded stress also affects the crack propagation, and the proportion becomes larger and larger with time. In the initial stage, the cracks in specimens B1 and B2 propagated along the negative x axis. At 28.56 μs, the horizontal velocities of the two specimens reached the extreme values of 89.9 m·s^{-1} and −105.3 m·s^{-1}, respectively. The crack continued to propagate along the x positive axis, and the v_x in specimen B2 reached the maximum more quickly than that of specimen B1. As can be seen from Figure 8a, when v_x is greater than 0, the area of the B1 curve is larger than that of specimen B2. This explains why the main crack in specimen B1 is more offset than that in specimen B2, as can be observed in Figure 4. Meanwhile, comparing the maximum peak velocity and curve area of specimen B1, the maximum peak velocity and curve area of specimen B2 are smaller, indicating that the preloaded compressive stress significantly suppresses the crack velocity in horizontal direction, and the pattern of the main crack in Figure 4 is further explained.

The vertical velocity v_y occupies the main position in the total crack propagation velocity. The change law of vertical velocity v_y in group B is comparable to that of DSIFs (Figure 6), as shown in Figure 8b. At the same time, the v_y curves of the two specimens are similar. In the initial stage, the v_y in specimen B1 and B2 increased rapidly to the maximum, which was 396.5 m·s^{-1} and 356.3 m·s^{-1}, respectively, indicating that preloaded stresses suppress the v_y. However, in the later stage, the v_y in specimen B1 is less than that in specimen B2, indicating that the preloaded stress promotes the v_y. This is because the angle between the preloaded stress and the crack propagation direction is different. At crack initiation, the preloaded stress is perpendicular to the crack direction. In the later stage, the preloaded stress is parallel to the crack propagation direction. With time, the effect of preloaded stress on cracks becomes more obvious. In addition, the crack initiation velocity also affects the whole process of crack propagation.

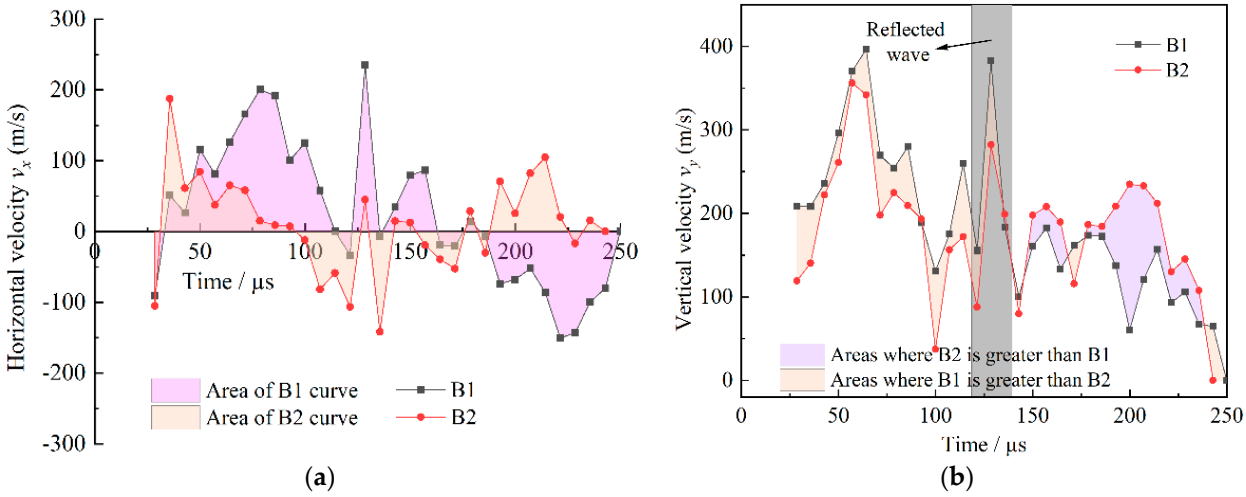

Figure 8. Horizontal and vertical velocities of main cracks in specimens B1 and B2 vs. time. (**a**) Horizontal speed. The red area represents the range of B1 curve and the yellow area represents the range of B2 curve of specimen. (**b**) Vertical velocity. The red area represents the range where the B1 curve is higher than the B2 curve; the yellow area represents the range where the B1 curve is lower than the B2 curve.

Figure 9 shows the curve of the crack velocity in specimens A2, B2, and C2 with time. The initial velocities in the three groups of specimens were 432.6 m·s^{-1}, 159.1 m·s^{-1}, and 117.5 m·s^{-1}, respectively. In Figure 9, the crack velocity oscillated with time, and the velocity oscillation trend was similar in all three specimens. Finally, the blast-induced cracks in specimens stopped at 264.2 μs, 242.8 μs, and 228.5 μs, respectively, indicating that the defect curvature can significantly affect the crack arrest time. The main crack propagation time at negative curvature defects is longer than that at positive curvature defects. From the overall data curve, the specimens with the main crack velocity arranged from large to small are A2, B2, and C2, indicating that the defect curvature can significantly affect the main crack velocity, and the negative curvature defect is more beneficial to the main crack propagation than the positive curvature defect. The crack velocity and time affect the crack length. The results also verify the difference of crack length among specimens A2, B2, and C2.

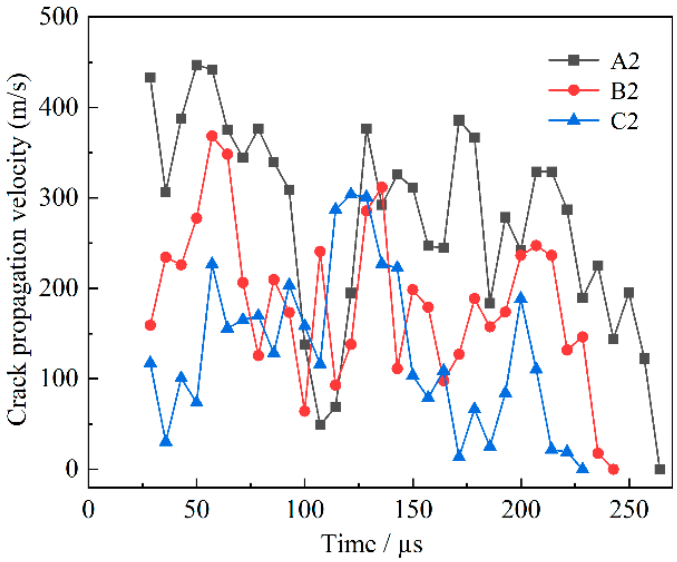

Figure 9. Crack propagation velocity at defects with different curvature.

3.1.4. Crack Initiation Angle

The main crack occurred at the end of the defect under blast-induced stress wave. As shown in Figure 10a, the angle between the end of the defect and the main crack was defined as the main crack initiation angle. In Figure 10a, the main crack at the right end of the defect in groups A and B was analyzed. There was no main crack in specimen C1, so the main crack at both ends of the defect was shown in specimen C2. The initiation angles of cracks C2-1 and C2-2 were about the same, which verified the repeatability of the experiment and the accuracy of the initiation angle. In the specimens with negative curvature defects, the initiation angle in specimen A1 (75.7°) was larger than that in specimen A2 (70.7°). In the defect with zero curvature, the initiation angle in specimen B1 (102.2°) was larger than that in specimen B2 (96.8°). The findings demonstrate that the preloaded stress reduces the initiation angle of the crack for specimens with negative or zero curvature defects. The compressive stress has less influence on the initiation angle, but the curvature has a great influence on the initiation angle. The initiation angle with negative curvature is smaller than that with zero curvature. For group C (the curvature is positive), the compressive stress promoted the occurrence of cracks in the defects, and the crack initiation position was not at the end of the defect. This is an interesting phenomenon, and it is further explained in the numerical analysis.

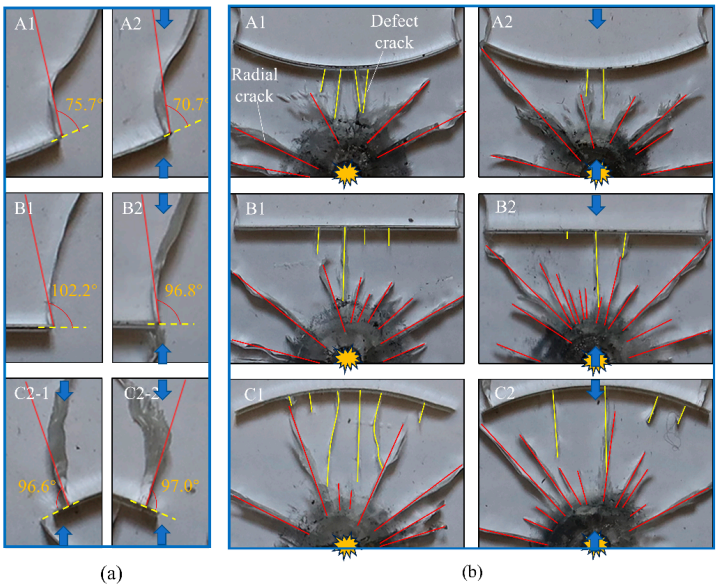

Figure 10. Local pictures of blast-induced cracks in each group of specimens. (**a**) The angle of crack initiation. (**b**) Crack distribution between blastholes and defects. The blue arrow represents the static stress and the orange polygon represents the blasting load.

3.2. Blast-Induced Damage Analysis

Figure 10b depicted the distribution of cracks between the defects and the blasthole. The damage degree of the specimen could be measured by the number and distribution of cracks. The crack distribution between the defect and the blasthole is mainly composed of two parts. One part is the 'defect crack' caused by reflected waves of the defect, and the other is the 'radial crack' caused by blast-induced stress wave. In Figure 10b, the defect crack on the defect was characterized by a yellow line, and the radial crack was characterized by a red line. At the same time, the furthest distance between yellow lines is defined as the distribution length of defect cracks. In the Figure 10b, most of the defect cracks were perpendicular to the defects, and most of the extension lines of the radial cracks passed through the blasthole. This is because blast-induced stress waves spread outward in a circle along the blasthole, forming radial cracks. The reflected tensile wave is formed when the blast-induced wave encounters defects, and reflection tensile cracks are further formed. Compared with the cracks in the same group of specimens, it was

known that the number and distribution length of defect cracks in specimens A1, B1, and C1 are larger than those in specimens A2, B2, and C2, indicating that compressive stress can reduce the damage degree of defects. However, the number of radial cracks in specimens A1, B1, and C1 is less than that in specimens A2, B2 and C2, indicating that preloaded stress can increase the number of radial cracks. This is because the area between the defect and the blasthole is parallel to the preloaded stress, and the preloaded stress changes the stress distribution around the blasthole and promotes the generation of radial cracks parallel to the compressive stress. Comparing cracks at different curvature defects, the curvature of the defect significantly affected the number and distribution length of the defect crack, and the order from small to large was specimens A2, B2, and C2 in that order. The biggest number of radial cracks were found in specimen B2, followed by specimen C2, and the smallest number were found in specimen A2. In addition, the specimens without compressive stress had the same law as the specimens under compressive stress. This is because the reflected wave at the defect affects the generation and propagation of defect cracks. This phenomenon would be further explored in the following research work.

3.3. The Defect Crack Initiation Mechanism

The blast-induced stress wave followed the 'Huygens principle' in the propagation [40]. Every point at which shock waves reached is the source of secondary waves, which traveled at the speed and frequency of the primary wave. The new wavefront was the envelope of these secondary waves. When waves encountered obstacles in the propagation, phenomena such as reflection, incidence, and interference would occur, resulting in new forms of propagation. A schematic diagram of waves encountering defects of different curvature was shown in Figure 11. The front end of the blast-induced stress wave was mainly a compression wave. As shown with the red curve in Figure 11, a reflected tensile wave was formed when the compressive wave met the free surface, resulting in a tensile crack. As the figure illustrates, the blast-induced stress wave met the defect for the first time at $t = t_2$; at $t = t_3$, reflected waves had been formed at the defect. The curvature of the defect affected the direction and range of reflected wave propagation. In $\Delta t = t_3 - t_2$, the range of reflected waves formed at different curvature defects from large to small were the specimens with C_{-25}, C_0, and C_{25}. Meanwhile, different curvatures also affected the angle of propagation direction between incident and reflected waves, and further affected the amplitude of stress wave in superposition. This also explains why the curvature of the defect significantly affects the number and distribution length of the defect crack.

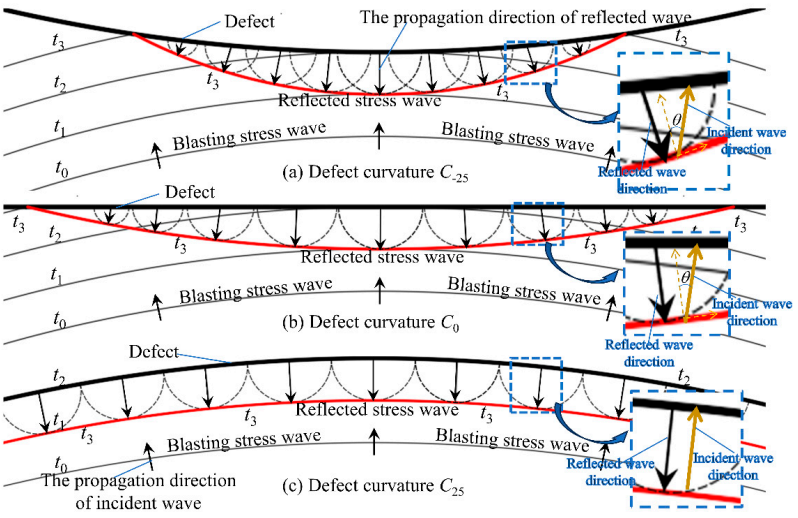

Figure 11. Stress wave propagation at different curvature defects. Red lines represent reflected waves; thick black lines represent defects.

4. Numerical Simulation

4.1. Numerical Model

In this section, the propagation process of blast-induced stress waves at different curvature defects under compressive stress was further studied. The commercial software ANSYS/LS-DYNA (R 18.0) was used to simulate detonation and stress wave propagation. The dimensions, material parameters, and boundary conditions of the numerical model are the same as those of the above experimental specimens. According to the curvature and boundary conditions of each model, the models were named as C_{-25}-0Mpa, C_0-0Mpa, C_{25}-0Mpa, C_{-25}-3Mpa, C_0-3Mpa, and C_{25}-3Mpa. The accuracy of the numerical simulation method and parameters had been verified by blasting experiments [3,41]. The model utilized a single-layer solid grid with a mesh size of 1 mm. The local grids at the defects and blastholes of group B model specimens are shown in Figure 12. The Lagrangian–Euler fluid–solid coupling algorithm was used for specimens, explosives, and air. The grid nodes of explosive and air are shared, and the specimen and air are coupled with each other. For the model under preloaded static stress, the static analysis was carried out first, and then the display dynamic calculation. In Table 1, the material properties of PMMA were displayed. The elastic–plastic model was used in the specimen without considering the damage. The density of air is 1.29×10^{-3} g/cm^3. The lead azide was selected for the explosive, and the JWL equation of state (Equation (4)) is used to simulate the detonation pressure P [42].

$$P = A_J(1 - \omega/R_1V)e^{-R_1V} + B_J(1 - \omega/R_2V)e^{-R_2V} + \omega E_0/V \tag{20}$$

where E_0 is specific internal energy; V is the volume of detonation products, and the parameters of JWL equation are A_J, B_J, R_1, R_2, and ω. Table 4 displays the required parameters of the explosive and its JWL equation.

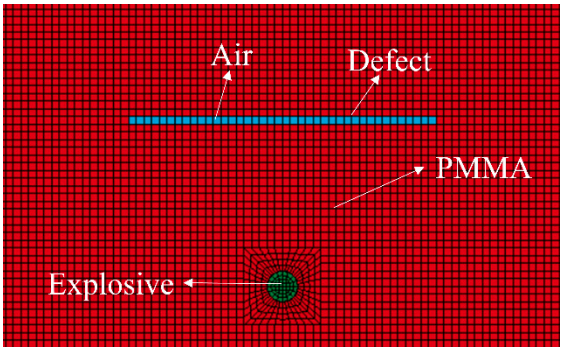

Figure 12. Grid of partial model. This is a group B grid model. The mesh size is 1 mm.

Table 4. Parameters of equation of explosives and the JWL.

Density ρ_0(g/cm^3)	Detonation Velocity (m/s)	A_J (GPa)	B_J (GPa)	R_1	R_2	ω
2.56	4478	436.3	26.46	5.68	2.01	0.697

4.2. Numerical Analysis Results

Figure 13 showed the compressive stress distribution of the specimens with defects under the pressure of 3 Mpa, that is, the compressive stress diagram at t = 0 μs. Tensile stress has a negative value while compressive stress has a positive value. Under the action of uniaxial pressure, the compressive stress concentration zone was produced at the end of the defect, and the tension concentration zone was produced in the middle of the defect and on the lower and upper sides of the blastholes. The curvature of defects affected the shape and size of the stress concentration zone, and further affected the crack initiation

and propagation. The preloaded stress changed the stress state around the blasthole and further changed the crack initiation and radial crack distribution of the blasthole.

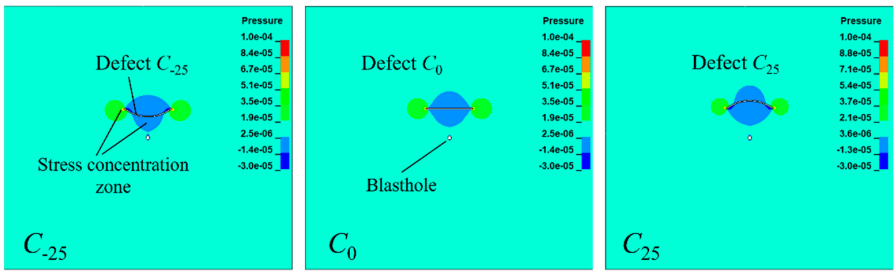

Figure 13. The compressive stress distribution of the specimen under 3 Mpa. Blue represents compressive stress; red represents tensile stress.

As seen in Figure 14, different curvatures had an impact on how the blast-induced stress wave propagated. The evolution process of the stress wave in specimens with defects can be clearly observed from Figure 14, and the results can improve the analysis of blast-induced fracture mechanism in specimens with defects. The evolution time of the stress wave in the numerical simulation is consistent with the experimental results of the caustics, further demonstrating the viability of the numerical method. After initiation, the propagation direction of the blast-induced wave changed when a defect was encountered, forming a reflected wave. At t = 18.7 µs, stress waves diffracted at the end of defects, and the stress concentration zone occurred at the end and the whole surface of the defect. This is the main reason for the formation of main cracks and defect cracks. It can be seen from the picture that the curvature of the defect affects the shape and size of the reflected wave at the defect, and the result is consistent with the theoretical diagram analysis in Section 3.3. This is also the main reason why different curvatures affect defect cracks and radial cracks. The blast-induced stress wave formed a reflected tensile wave at the boundary, which further affected the propagation of the main crack.

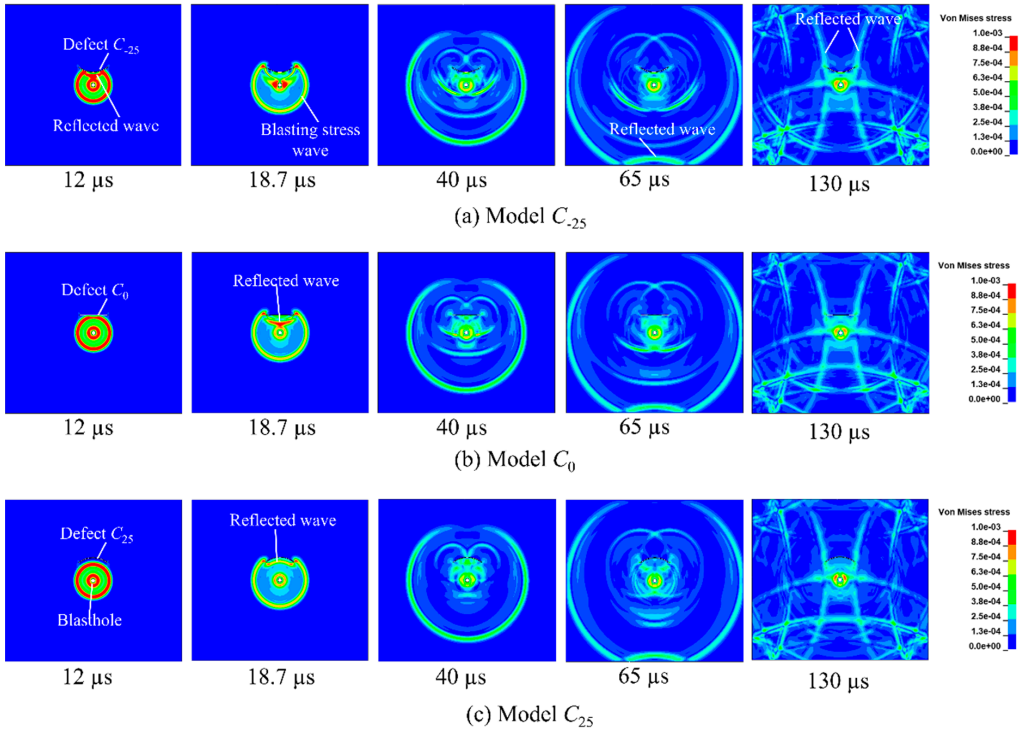

Figure 14. Mises stress diagram of stress wave propagation under compressive stress.

To further explore the reasons for the difference of the main crack of each specimen, the maximum principal stress of the monitoring point at the defect end was extracted and analyzed from the point of view of stress wave, as shown in Figure 15. The stress of the monitoring point at the end of the defect was affected by the curvature. In the models C_{-25} and C_0, there was a large tensile stress at the end of the defects under stress waves. However, the blast-induced stress wave had little effect on the defects of C_{25}. Therefore, there was a main crack at the defect end of C_{-25} and C_0, but there was no main crack at the defect end of C_{25}. In addition, the maximum principal stress of the C_{-25} monitoring point is the largest, while that of the C_{25} monitoring point is the smallest. This indicates that the smaller the curvature of the defect, the higher the tensile stress of the monitoring point, and the easier it is for cracks to initiate and propagate at the end of the defect. According to the caustic spots and the tensile stress at the end of the defect, the main crack is mainly caused by tensile failure. When the tensile stress exceeds its tensile strength, the end of the defect begins to fracture.

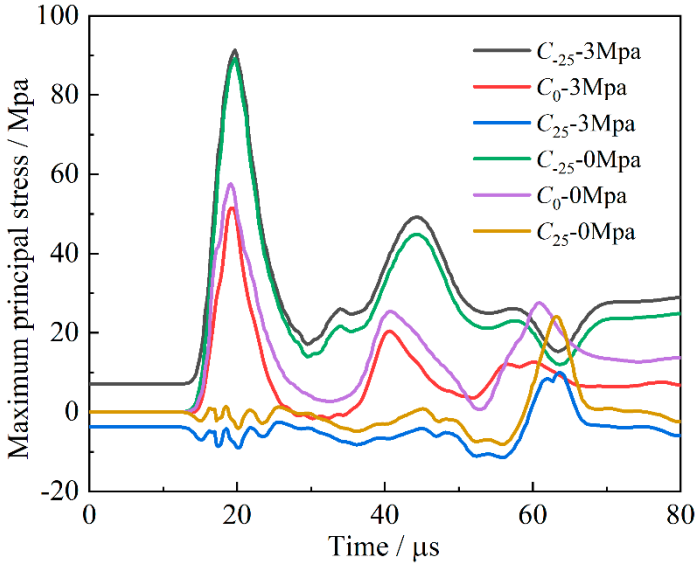

Figure 15. Maximum principal stress at the end of the defect with time. The stress curve of 0–80 us is shown in blasting.

The influence of compressive stress on the end of the defect with different curvatures was different before the action of the blast-induced stress wave. In model C_{-25}, the compressive stress significantly increased the tensile stress of the monitoring point, while in model C_0, the compressive stress had little effect on the monitoring point. In model C_{25}, the preloaded stress could increase compressive stresses at the monitoring point. During the stress wave, the preloaded stress increased tensile stresses at the monitoring point in model C_{-25}, but reduced the tensile stress of the monitoring point in model C_0. In addition, the preloaded stress increased the compressive stress of the monitoring point in model C_{25}. This explains why the DSIFs of the B2 specimen are smaller than those of the B1 specimen in the crack initiation stage. The findings demonstrate that compressive stress can promote the crack initiation of defects with curvatures of -25 m^{-1}, but inhibit the crack initiation of defects with curvatures of 0 m^{-1} and 25 m^{-1}. However, compared with the stress wave, the influence of compressive stress is smaller.

To analyze the reason why the crack initiation position in specimen C2 was not at the end of the defect, the maximum principal stresses at three monitoring points (a, b, and c) in the model C_{25}-3Mpa were extracted (Figure 16). The three points (a, b, and c) were on the defect which is 0 mm, 1 mm, and 2 mm away from the end of the defect. The maximum tensile stress was not at the end of the defect. When the tensile stress at a certain point reached the tensile strength of the PMMA specimen, the point was fractured. The main

reason for the result is the reflected tensile wave on the upper surface of the defect and the diffraction of the explosive stress wave at the end of the defect.

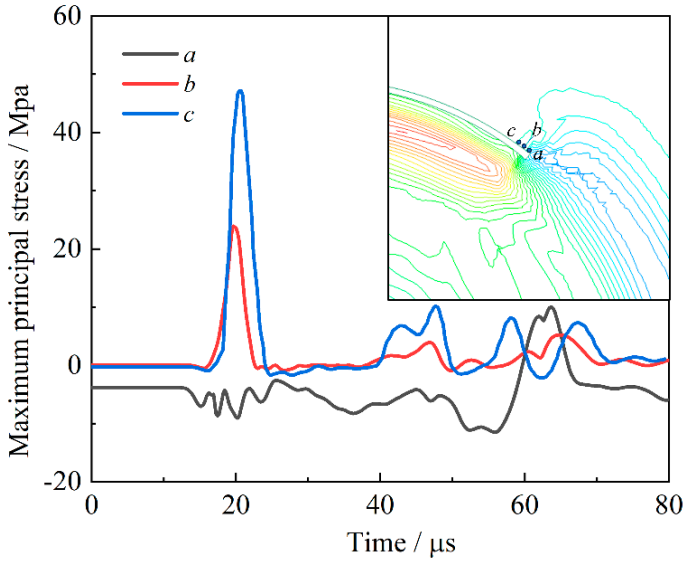

Figure 16. Maximum principal stress of model C_{25}-3Mpa at monitoring point a–c.

5. Application and Discussion

The scope of this study is limited to the model experiments with uniaxial preloaded condition. There are various shapes of joints in rock mass, and three representative shapes are selected in this paper. The blast-induced fracture was significantly influenced by the curvature of defect. For example, Li et al. [23] studied the effect of defect curvature radius on the blast-induced crack, but the influence of curvature on the main crack at the end of the defect was not analyzed, and the preloaded stress was not considered. In addition, on this basis, the influence of the curvature on the damage between the blasthole and the defect was also explored in this study. In deep engineering blasting, the influence of defect curvature on blast-induced fracture is more worthy of attention than that of compressive stress. For the rock mass with negative curvature defects, the damage area on the blasting side is relatively small, and the charge can be increased accordingly to increase the crushing effect. For rock mass with positive curvature defects, it is the opposite.

In the presplitting blasting, if possible, it is suggested that contour hole blasting should be used to form the defect contour to reduce the damage for the retained medium. In addition, the contour hole net should be arranged according to the shape of a positive curvature rather than a negative curvature. The design can improve the fragmentation of rock. In bench blasting, a bench contour with a positive curvature free surface can also promote the blasting effect. Therefore, the arrangement of a curved (positive curvature) hole net is also helpful to improve the blasting effect.

6. Conclusions

In this study, the blast-induced crack behavior and stress wave propagation of media with different curvature defects under preloaded stress were studied by experimental and numerical methods. The main conclusions are as follows:

(1) The blast-induced wave promoted the initiation of the crack at the end of the defect and controlled the direction of crack propagation. At the same time, the reflected wave could increase the crack velocity and DSIFs. The preloaded stress could mainly restrain the crack propagation in the horizontal direction, and the effect of preloaded stress was more significant with time. The effects of preloaded stress on the ends of defects with different curvature were different. In the early stage, the compressive stress could promote the fracture at the end of the defect with curvature of $-25\ m^{-1}$,

but inhibit the fracture at the end of the defect with curvature of 0 m^{-1} and 25 m^{-1}. In the later stage of blasting, preloaded compressive stresses promoted the propagation of the main crack. Meanwhile, compressive stress could reduce the crack initiation angle and damage degree at the defects, but increase the number of radial cracks between the blasthole and the defect. For specimens C_{-25} and C_0, the preloaded stress reduced the crack initiation angle by 5° and 5.4°, and reduced two and one defect cracks, respectively. For specimen C_{25}, the preloaded stress reduced two defect cracks.

(2) The defect curvature significantly affected the main crack propagation. The blast-induced wave changed the tensile stress at the end of the defect with different curvature, and then affected the DSIFs, crack propagation velocity, and crack initiation angle at the end of the defect with different curvature. The smaller the curvature of the defect, the higher the tensile stress of the monitoring point, and the easier it is for cracks to initiate and propagate. Compared with the main crack with zero curvature defect, the DSIFs, velocity, crack arrest time, crack length, and horizontal offset distance of the main crack with negative curvature defect were larger. The initiation angle of the main crack with a negative curvature defect was smaller than that with zero curvature defect. However, the end of the positive curvature defect did not crack. In addition, the curvatures of the defect affected the damage of the defect, which from low to high were C_{-25}, C_0 and C_{25}.

(3) The curvature of the defect has a greater effect on the initiation angle of the main crack, the crack propagation length, the crack velocity, the DSIFs, and the damage degree of the defect compared to preloaded static stress.

Author Contributions: Conceptualization, L.Y.; formal analysis, B.Y.; funding acquisition, L.Y.; methodology, C.H.; supervision, L.Y.; validation, X.G.; visualization, C.H.; writing—original draft, C.H.; writing—review and editing, Z.-X.Z. and A.A. All authors have read and agreed to the published version of the manuscript.

Funding: This work is supported by the National Natural Science Foundation of China (No. 52227805) and the Fundamental Research Funds for the Central University (No. 2022JCCXLJ01 and No. 2023ZKPYLJ04).

Data Availability Statement: The data presented in this study are available on request from the corresponding author. The data are not publicly available due to restrictions eg privacy or ethical.

Conflicts of Interest: The authors declare no conflict of interest.

References

1. Zhang, Z.X. *Rock Fracture and Blasting: Theory and Applications*; Butterworth-Heinemann: Oxford, UK, 2016.
2. He, L.; Kong, D.; Lei, Z. Research on Vibration Propagation Law and Dynamic Effect of Bench Blasting. *Mathematics* **2022**, *10*, 2951. [CrossRef]
3. Huang, C.; Zhang, Z.-X.; Yang, L.; Aladejare, A.; Gao, Z.; Li, Q. Effect of prestress on propagation of blasting-induced main crack in specimens with empty hole. *Theor. Appl. Fract. Mech.* **2023**, *126*, 103928. [CrossRef]
4. Xia, Y.; Liu, B.; Li, T.; Zhao, D.; Liu, N.; Tang, C.; Chen, J. Numerical Simulation of Failure Modes in Irregular Columnar Jointed Rock Masses under Dynamic Loading. *Mathematics* **2023**, *11*, 3790. [CrossRef]
5. Chen, C.; Yang, R.; Xu, P.; Ding, C. Experimental study on the interaction between oblique incident blast stress wave and static crack by dynamic photoelasticity. *Opt. Lasers Eng.* **2021**, *148*, 106764. [CrossRef]
6. Yang, R.S.; Ding, C.X.; Yang, L.Y.; Chen, C.; Sun, J.C. Tests for structures with flaws under impact loading. *J. Vib. Shock.* **2016**, *35*, 103–108. [CrossRef]
7. Yang, R.; Xu, P.; Yue, Z.; Chen, C. Dynamic fracture analysis of crack–defect interaction for mode I running crack using digital dynamic caustics method. *Eng. Fract. Mech.* **2016**, *161*, 63–75. [CrossRef]
8. Lu, W.; Chen, M.; Geng, X.; Shu, D.; Zhou, C. A study of excavation sequence and contour blasting method for underground powerhouses of hydropower stations. *Tunn. Undergr. Space Technol.* **2012**, *29*, 31–39. [CrossRef]
9. Kutter, H.; Fairhurst, C. On the fracture process in blasting. *Int. J. Rock Mech. Min. Sci. Géoméch. Abstr.* **1971**, *8*, 181–202. [CrossRef]
10. Rossmanith, H.P.; Knasmillner, R.E.; Daehnke, A.; Mishnaevsky, L., Jr. Wave propagation, damage evolution and dynamic fracture extension. *Part II. Blasting. Mater. Sci.* **1996**, *32*, 403–410.
11. Yang, L.; Yang, A.; Chen, S.; Fang, S.; Huang, C.; Xie, H. Model experimental study on the effects of in situ stresses on pre-splitting blasting damage and strain development. *Int. J. Rock Mech. Min. Sci.* **2021**, *138*, 104587. [CrossRef]

12. Li, Q.; Xu, W.; Wang, K.; Gao, Z.; Huo, S.; Huang, C. Study on the mechanical behavior of crack propagation effect at the end of de-fect under explosive load. *Int. J. Rock Mech. Min. Sci.* **2021**, *138*, 104624. [CrossRef]
13. Zhu, Z.; Mohanty, B.; Xie, H. Numerical investigation of blasting-induced crack initiation and propagation in rocks. *Int. J. Rock Mech. Min. Sci.* **2007**, *44*, 412–424. [CrossRef]
14. Yao, X.F.; Jin, G.C.; Arakawa, K.; Takahashi, K. Experimental studies on dynamic fracture behavior of thin plates with parallel single edge cracks. *Polym. Test.* **2002**, *21*, 933–940. [CrossRef]
15. Wang, Y.; Dong, J.; Wang, Z.; Zhao, Y. Analysis of the expansion process of cracks caused by blasting stress waves in a PMMA medium with filled defects. *Mater. Today Commun.* **2021**, *27*, 102396. [CrossRef]
16. Xu, P.; Yang, R.; Guo, Y.; Guo, Z. Investigation of the Blast-Induced Crack Propagation Behavior in a Material Containing an Unfilled Joint. *Appl. Sci.* **2020**, *10*, 4419. [CrossRef]
17. Mellal, F.; Bennai, R.; Nebab, M.; Atmane, H.A.; Bourada, F.; Hussain, M.; Tounsi, A. Investigation on the effect of porosity on wave propagation in FGM plates resting on elastic foundations via a quasi-3D HSDT. *Waves Random Complex Media* **2021**, 1–27. [CrossRef]
18. Dahmane, M.; Benadouda, M.; Fellah, A.; Saimi, A.; Hassen, A.A.; Bensaid, I. Porosities-dependent wave propagation in bi-directional functionally graded cantilever beam with higher-order shear model. *Mech. Adv. Mater. Struct.* **2023**, 1–11. [CrossRef]
19. Mellal, F.; Bennai, R.; Avcar, M.; Nebab, M.; Atmane, H.A. On the vibration and buckling behaviors of porous FG beams resting on variable elastic foundation utilizing higher-order shear deformation theory. *Acta Mech.* **2023**, *234*, 3955–3977. [CrossRef]
20. Yahia, S.A.; Atmane, H.A.; Houari, M.S.A.; Tounsi, A. Wave propagation in functionally graded plates with porosities using various higher-order shear deformation plate theories. *Struct. Eng. Mech.* **2015**, *53*, 1143–1165. [CrossRef]
21. Ayache, B.; Bennai, R.; Fahsi, B.; Fourn, H.; Atmane, H.A.; Tounsi, A. Analysis of wave propagation and free vibration of functionally graded porous material beam with a novel four variable refined theory. *Earthq. Struct.* **2018**, *15*, 369.
22. Ding, C.-X.; Yang, R.-S.; Chen, C.; Ma, X.-M.; Kang, Y.-X.; Zhao, Y. Experimental study on the interaction between directional crack and opening joint in slotted charge blasting. *J. Eng. Sci. (Chin.)* **2021**, *43*, 894–902.
23. Li, C.; Kang, Y.; Zhang, Y.; Xiao, C. Analyze the influence of explosion stress wave on the dynamic fracture of PMMA plates with different curvature radius defects. *Int. J. Solids Struct.* **2021**, *234–235*, 111278. [CrossRef]
24. Yan, G.; Zhang, F.; Ku, T.; Hao, Q. Experimental study on failure mechanism and geometric parameters of blasting crater under uniaxial static compressive stresses. *Bull. Eng. Geol. Environ.* **2022**, *81*, 251. [CrossRef]
25. Yan, G.; Zhang, F.; Ku, T.; Hao, Q.; Peng, J. Experimental Study and Mechanism Analysis on the Effects of Biaxial In-Situ Stress on Hard Rock Blasting. *Rock Mech. Rock Eng.* **2023**, *56*, 3709–3723. [CrossRef]
26. Yang, L.-Y.; Ding, C.-X. Fracture mechanism due to blast-imposed loading under high static stress conditions. *Int. J. Rock Mech. Min. Sci.* **2018**, *107*, 150–158. [CrossRef]
27. Yang, R.; Ding, C.; Li, Y.; Yang, L.; Zhao, Y. Crack propagation behavior in slit charge blasting under high static stress conditions. *Int. J. Rock Mech. Min. Sci.* **2019**, *119*, 117–123. [CrossRef]
28. Zhou, Z.; Chen, Z. Numerical Analysis of Dynamic Responses of Rock Containing Parallel Cracks under Combined Dynamic and Static Loading. *Geofluids* **2020**, *2020*, 2948135. [CrossRef]
29. Yang, L.; Yang, R.; Qu, G.; Zhang, Y. Caustic study on blast-induced wing crack behaviors in dynamic–static su-perimposed stress field. *Int. J. Rock Mech. Min. Sci.* **2014**, *24*, 417–423.
30. Yang, R.; Ding, C.; Yang, L.; Chen, C. Model experiment on dynamic behavior of jointed rock mass under blasting at high-stress conditions. *Tunn. Undergr. Space Technol.* **2018**, *74*, 145–152. [CrossRef]
31. Wei, C.X.; Zhu, W.C.; Bai, Y. Numerical simulation of blasting of jointed rock mass under different ground stress conditions. *J. Eng. Sci.* **2016**, *38*, 19–25.
32. Wang, Z.; Konietzky, H. Modelling of blast-induced fractures in jointed rock masses. *Eng. Fract. Mech.* **2009**, *76*, 1945–1955. [CrossRef]
33. Yue, W.Y.; Li, J.G.; Chai, X.W. Analysis and study on the influence of ground stress on blasting of fractured rock mass. *Blasting* **2021**, *38*, 51–57.
34. Yang, L.; Huang, C.; Bao, S.; Zhang, L. Model experimental study on controlled blasting of slit charge in deep rock mass. *Soil Dyn. Earthq. Eng.* **2020**, *138*, 106318. [CrossRef]
35. Qiu, P. Mechanisms of the Interaction between Blast Stress Waves and Cracks. Ph.D. Thesis, China University of Mining & Technology-Beijing, Beijing, China, 2020.
36. Theocaris, P.; Papadopoulos, G. Elastodynamic forms of caustics for running cracks under constant velocity. *Eng. Fract. Mech.* **1980**, *13*, 683–698. [CrossRef]
37. Rosakis, A.J. Analysis of the optical method of caustics for dynamic crack propagation. *Eng. Fract. Mech.* **1980**, *13*, 331–347. [CrossRef]
38. Papadopoulos, G.A. *Fracture Mechanics. The Experimental Method of Caustics and The Det.-Criterion of Fracture*; Springer: New York, NY, USA, 1993.
39. Zhang, Q.B.; Zhao, J. Effect of loading rate on fracture toughness and failure micro-mechanisms in marble. *Eng. Fract. Mech.* **2013**, *102*, 288–309. [CrossRef]

40. Liu, C.; Lu, Y.; Xia, B.; Yu, P. Directional fracturing by slotting-blasting-caused stress wave form changes. *Int. J. Impact Eng.* **2019**, *129*, 141–151. [CrossRef]
41. Xu, W.L. Experimental Study on Explosion Dynamic Characteristics and Crack Propagation of Rock Materials with Defects. Ph.D. Thesis, China University of Mining and Technology, Beijing, China, 2021.
42. Alia, A.; Souli, M. High explosive simulation using multi-material formulations. *Appl. Therm. Eng.* **2006**, *26*, 1032–1042. [CrossRef]